ACS OMEGA

http://pubs.acs.org/journal/acsodf

Article

Synthesis and Characterization of a Multication Doped Mn Spinel, $LiNi_{0.3}Cu_{0.1}Fe_{0.2}Mn_{1.4}O_4$, as 5 V Positive Electrode Material

Priyanka Sharma, Chittaranjan Das, Sylvio Indris, Thomas Bergfeldt, Liuda Mereacre, Michael Knapp, Udo Geckle, Helmut Ehrenberg, and Mariyam Susana Dewi Darma*

Cite This: *ACS Omega* 2020, 5, 22861−22873

Read Online

ACCESS | Metrics & More | Article Recommendations | Supporting Information

ABSTRACT: The suitability of multication doping to stabilize the disordered $Fd\bar{3}m$ structure in a spinel is reported here. In this work, $LiNi_{0.3}Cu_{0.1}Fe_{0.2}Mn_{1.4}O_4$ was synthesized via a sol−gel route at a calcination temperature of 850 °C. $LiNi_{0.3}Cu_{0.1}Fe_{0.2}Mn_{1.4}O_4$ is evaluated as positive electrode material in a voltage range between 3.5 and 5.3 V (vs Li^+/Li) with an initial specific discharge capacity of 126 mAh g^{-1} at a rate of $C/2$. This material shows good cycling stability with a capacity retention of 89% after 200 cycles and an excellent rate capability with the discharge capacity reaching 78 mAh g^{-1} at a rate of 20C. *In operando* X-ray diffraction (XRD) measurements with a laboratory X-ray source between 3.5 and 5.3 V at a rate of $C/10$ reveal that the (de)lithiation occurs via a solid-solution mechanism where a local variation of lithium content is observed. A simplified estimation based on the *in operando* XRD analysis suggests that around 17−31 mAh g^{-1} of discharge capacity in the first cycle is used for a reductive parasitic reaction, hindering a full lithiation of the positive electrode at the end of the first discharge.

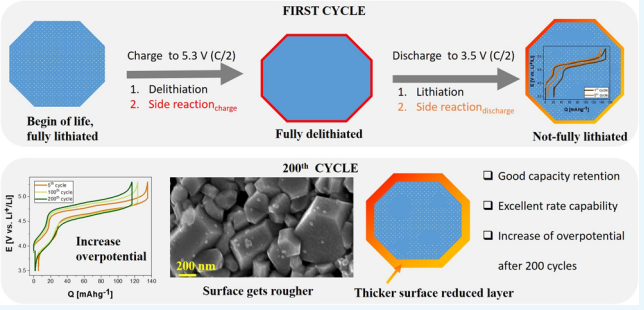

INTRODUCTION

The rapid development in the electric automobile and energy sectors has led to the demand for improved lithium-ion batteries (LIBs). Since the electrochemical performance of a battery is mostly limited by its positive electrode, materials with high rate capability, specific capacity, and long cycling life are required. Recently, $LiNi_{0.5}Mn_{1.5}O_4$ (LNMO) spinels have gained much attention due to their high operating potential, environmental friendliness, low cost, and good thermal stability.[1−7] However, their electrochemical properties are dependent on the crystal structure. It has been previously reported that LNMO with a disordered $Fd\bar{3}m$ structure shows better electrochemical performance than the ordered ($P4_332$) structure. It is argued in the literature[7] that a perfectly cation-ordered spinel with a space group of $P4_332$ resists the solid-solution phase transition behavior because the Ni/Mn ordering is incompatible with the ordering of Li^+ and vacancies during delithiation, whereas the introduction of Ni/Mn disordering into the spinel structure results in a gradual increase in stability for a solid-solution reaction. This leads to improvement in the electrochemical properties by reducing the mechanical stress/strain due to lattice mismatches in the absence of a single-phase process. Nevertheless, the disordered structure is obtained at higher temperatures, which is accompanied by oxygen loss and formation of rock salt impurities like $Li_xNi_{1-x}O/Ni_6MnO_8$.[8]

Elemental doping is considered to suppress impurity formation and enhance electrochemical performance. Doping modifications such as cation doping (Na,[9] Al,[10] Cr,[11] Fe,[12] Cu,[13] Sm,[14] Zr,[15] Nb,[16] Mo,[17] etc.), anion doping (S,[18] P[19]), or composite doping[20] of LNMO are amply reported. Among various cation substitutions, Fe influences the electrochemistry of spinels favorably.[12,21,22] In the previous work carried out in our group, it was found that the introduction of a small quantity of Fe in LNMO led to improvements in electrochemical performance owing to the suppression of Ni_6MnO_8 in addition to reduced strain due to a dominant single-phase cycling process.[23] The best cycling performance of $LiNi_{0.5-x}Fe_{2x}Mn_{1.5-x}O_4$ was found for x = 0.1. However, this material system still required a calcination temperature of 1000 °C to obtain the cation-disordered structure. Therefore, as a further step of a multication doping strategy, the influence of partial substitution of Ni by Cu in the parent compound is investigated. Multication doping is considered to increase entropy in the system, which might lead to the stabilization of a disordered spinel at lower temperatures. Following this

Received: May 10, 2020
Accepted: July 23, 2020
Published: August 31, 2020

approach, we report the synthesis and characterization of a $LiNi_{0.3}Cu_{0.1}Fe_{0.2}Mn_{1.4}O_4$ spinel. The characterization results show the successful formation of a disordered spinel at a temperature of 850 °C, which is lower than the synthesis temperature of the parent compound $LiNi_{0.4}Fe_{0.2}Mn_{1.4}O_4$. The cycling mechanism has also been studied and follows a solid-solution process.

RESULTS AND DISCUSSION

This section is organized into four parts: characterization of as-synthesized $LiNi_{0.3}Cu_{0.1}Fe_{0.2}Mn_{1.4}O_4$, electrochemical performance of $LiNi_{0.3}Cu_{0.1}Fe_{0.2}Mn_{1.4}O_4$ (calcined at 850 °C) as positive electrode material, surface analysis by X-ray photoelectron spectroscopy (XPS), and mechanism of lithium (de)intercalation.

Characterization of As-Synthesized $LiNi_{0.3}Cu_{0.1}Fe_{0.2}Mn_{1.4}O_4$. In this section, the elemental composition, morphology, crystal structure, and local environment of lithium of as-synthesized materials are elaborated using different methods, which include Inductively coupled plasma and optical emission spectrometry (ICP-OES), scanning electron microscopy (SEM), X-ray diffraction (XRD), Raman spectroscopy, and NMR spectroscopy.

The elemental analyses of the sample calcined at 850 °C are given in Table 1. The chemical composition of the sample, obtained from ICP-OES, is $LiNi_{0.3}Cu_{0.1}Fe_{0.19}Mn_{1.41}O_4$, which is quite close to the composition calculated based on the stoichiometric amount of the corresponding precursors ($LiNi_{0.3}Cu_{0.1}Fe_{0.2}Mn_{1.4}O_4$).

Table 1. ICP-OES and carrier gas hot extraction (CGHE) Analyses of $LiNi_{0.3}Cu_{0.1}Fe_{0.2}Mn_{1.4}O_4$ Calcined at 850 °C

element	wt %	standard deviation	measurement accuracy
Li	3.6	0.03	0.09
O	33.6	0.6	2.92
Mn	42.55	0.11	0.89
Fe	5.46	0.02	0.12
Ni	9.52	0.01	0.2
Cu	3.44	0.01	0.13
total wt %	98.17		

SEM images of the powder before and after calcination are shown in Figure 1a,b, respectively. The precursor dried at 400 °C lacks well-defined edges with particle sizes in the range of 20−80 nm. The particle sizes for the calcined sample range from 300 nm to 1 μm. The crystallized particles have a truncated polyhedral shape which might be a result of the dopants. It has been shown that truncated {100} surfaces in LNMO improve the diffusivity of Li^+ ions and stabilize interfacial behavior.[25] Therefore, an increase in the ratio of (100) to (111) facets can improve cycling stability and rate capability.

Figure 1c shows XRD patterns for the powder before and after calcination. The diffraction data for both samples reveal the formation of a cubic spinel phase with an $Fd\bar{3}m$ space group as the main phase. The lattice parameters for the uncalcined and calcined samples are calculated as 8.1829(2) and 8.2046(3) Å, respectively. The lattice parameter of the calcined sample is larger than that of the uncalcined sample, which can be explained by the reduction of Mn^{4+} to Mn^{3+} with a larger ionic radius due to oxygen deficiency.[26] Li_2MnO_3 with a layered structure ($C2/m$) appears as 2.6(6) wt % impurity for the calcined sample as shown in Figure 1c, obtained from Rietveld refinement. The impurity phase might be formed due to the oxygen loss at elevated temperatures. When the oxygen loss becomes significant, the spinel decomposes and forms an oxygen-deficient spinel and Li_2MnO_3.[27] For this class of material, XRD is frequently used to predict the structural stability of the system, i.e., by evaluating the relative integrated intensity of the 311 reflection with respect to the 400 reflection (I_{311}/I_{400}), which is related to the degree of tetragonal ($[M]_2O_4$) distortion in the spinel framework. For a good structural stability and enhanced cycling retention, this ratio should be in the range of 0.96−1.10.[28] The ratio of I_{311}/I_{400} for the spinel calcined at 850 °C is 1.01, which lies within this range.

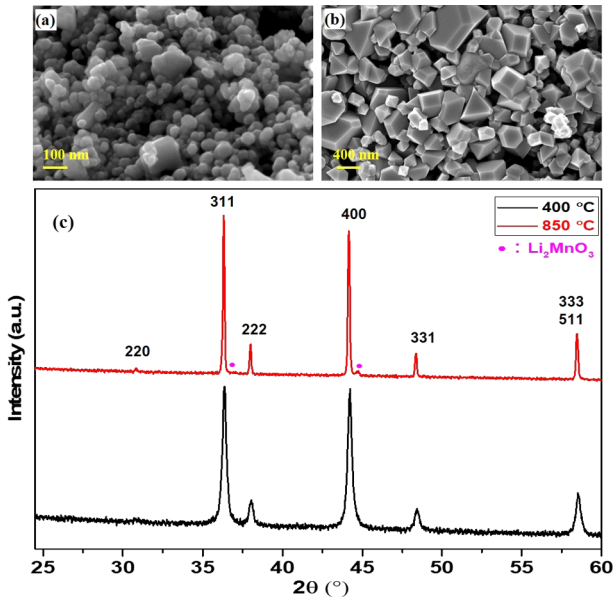

Figure 1. SEM images of (a) uncalcined (dried at 400 °C) and (b) calcined (850 °C) powder samples. (c) XRD patterns for uncalcined (dried at 400 °C) and (b) calcined (850 °C) powder samples.

The stabilization of the $Fd\bar{3}m$ phase can be related to the increased entropy in the system due to the incorporation of multiple cations. The configurational entropy, ΔS_{mix}, for the present system is computed as $1.24R$ (R is the universal gas constant), which lies within the range of medium entropy oxides (MEOs).[29] Such a high value of ΔS_{mix} might be responsible for suppressing cation ordering (and forming a more stable structure of $Fd\bar{3}m$).

Mn-based spinels can also be formed as an ordered phase exhibiting $P4_332$ symmetry. This $P4_332$ symmetry is marked by the presence of additional weak reflections at $2\theta \approx 15.3$, 39.7, 45.7, and 57.5°. These reflections are not observed for the calcined sample presented here, suggesting the formation of crystalline material in $Fd\bar{3}m$ symmetry. However, XRD cannot exclude the formation of an amorphous phase or a very low amount of impurities. Further investigation of the crystal structure was done by Raman spectroscopy, which can be used to characterize both crystalline and amorphous phases. Raman spectra between 100 and 1000 cm^{-1} from both the uncalcined sample dried at 400 °C and calcined sample at 850 °C are plotted and indexed in Figure 2a. The samples reveal broad bands at approximately 633 cm^{-1} (A_{1g}), 590 cm^{-1} (F_{2g}), 490 cm^{-1} (F_{2g}), 390 cm^{-1} (E_g), 208 cm^{-1} (vw), and 158 cm^{-1} (s). Mn−O stretching corresponds to the strong signal of the A_{1g}

https://dx.doi.org/10.1021/acsomega.0c02174
ACS Omega 2020, 5, 22861−22873

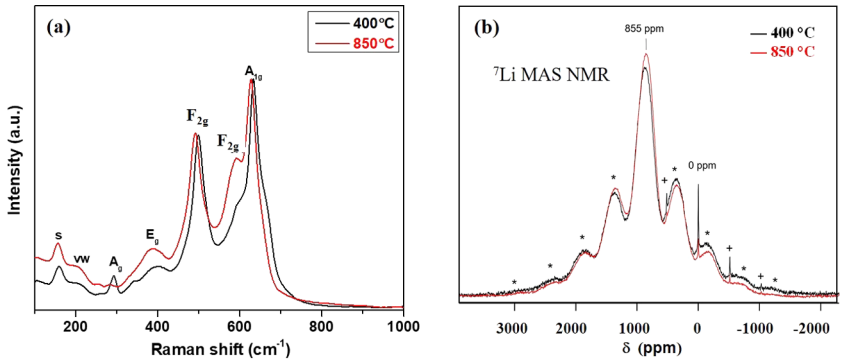

Figure 2. (a) Raman and (b) ^{7}Li MAS NMR spectra of the (uncalcined) sample dried at 400 °C and the sample calcined at 850 °C.

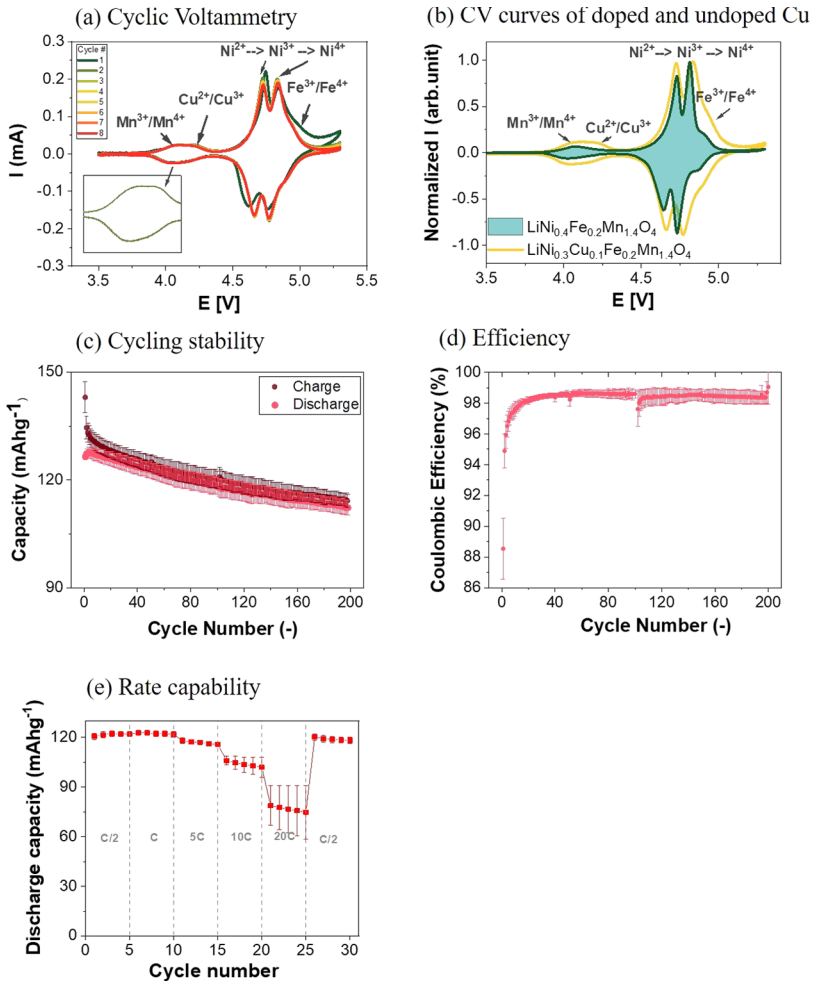

Figure 3. Cyclic voltammetry at a sweep rate of 0.1 mV s^{-1} for (a) the first eight cycles of $LiNi_{0.3}Cu_{0.1}Fe_{0.2}Mn_{1.4}O_4$ (b) fifth cycle of undoped $LiNi_{0.4}Fe_{0.2}Mn_{1.4}O_4$ (taken from Figure 5b in ref 23) and doped $LiNi_{0.3}Cu_{0.1}Fe_{0.2}Mn_{1.4}O_4$ for comparison. (c) Cycling stability (charge/discharge rate of C/2), (d) Coulombic efficiency, and (e) rate capability of $LiNi_{0.3}Cu_{0.1}Fe_{0.2}Mn_{1.4}O_4$ calcined at 850 °C within a voltage window of 3.5−5.3 V. Three samples were used for cycling stability test whereas two samples were used for the rate capability test. The standard deviation reflects the spread in the measured capacities.

band (the symmetric Mn−O stretching vibration of MnO_6 octahedra) and the broad signal of F_{2g}.[30] The peak positions of the material reported here deviate slightly compared to the values reported in literature, which can be attributed to the nature and concentration of the dopant ions used. In the case of cation ordering, splitting of the F_{2g} band at 590 cm^{-1} has been reported.[31] The absence of such a splitting further confirms the formation of a structure with $Fd\bar{3}m$ symmetry in the investigated system. The peak at 300 cm^{-1} in the uncalcined sample is identified as the A_g CuO phonon peak.[32] The absence of CuO reflections in the XRD pattern of the uncalcined sample is due to its low amount. Interestingly, the A_g CuO phonon peak is not observed for the sample calcined at 850 °C in Figure 2, suggesting that Cu has successfully been incorporated into the spinel lattice during calcination. The peaks (A_{1g}, F_{2g}) observed for the high-

https://dx.doi.org/10.1021/acsomega.0c02174
ACS Omega 2020, 5, 22861−22873

temperature sample are slightly shifted toward lower frequencies as compared to the uncalcined powder. The lattice parameter is increased at this calcination temperature. Consequently, the bond lengths of Mn−O and Ni−O bonds become longer, resulting in the corresponding Raman peaks at lower frequencies. To ensure a representative result, Raman mapping of both the samples was done (see Figure S3 in the Supporting Information). Weak peaks at around 400 cm^{-1} in the Raman mapping of the calcined sample are observed in a nonsystematic appearance; this might be caused by the very small and randomly distributed Li_2MnO_3 impurity.[33]

The local environment of lithium was investigated by ^{7}Li MAS NMR. Figure 2b shows ^{7}Li MAS NMR spectra of the two samples. The spinning side bands of the isotropic peaks at 855 and 0 ppm are marked with * and +, respectively. The two spectra look very similar except for the small peak near 0 ppm, which belongs to a diamagnetic impurity, most likely Li_2CO_3. The origin of this phase could be attributed to the organic compounds used during the sol−gel synthesis. A broad peak at 855 ppm dominates the spectra. The width results from the many different transition metals and consequently many different local environments around Li in the system. The position of this peak at 855 ppm is consistent with the values already reported for pure and Fe-doped LNMO.[23] The absence of other signals confirms that Li^+ is located exclusively on tetrahedral sites in the spinel structure.

Electrochemical Performances of $LiNi_{0.3}Cu_{0.1}Fe_{0.2}Mn_{1.4}O_4$. The electrochemical performance of $LiNi_{0.3}Cu_{0.1}Fe_{0.2}Mn_{1.4}O_4$ positive electrode material was evaluated from cyclic voltammetry (CV) and galvanostatic cycling at different charge rates. CV curves of this positive electrode are plotted in Figure 3a, showing that the general shape of the CV curves is preserved for the first eight cycles. However, it is also obvious from this figure that the position, width, and intensity of the peaks between 4.5 and 5.3 V in the first cycle are slightly different from the successive cycles, indicating that the lithiation mechanism of the first cycle might not be the same as for the following cycles. This small deviation is further investigated with *in operando* XRD measurements.

Figure 3b shows a comparison between the CV curve of the parent compound of $LiNi_{0.4}Fe_{0.2}Mn_{1.4}O_4$, which was synthesized without Cu doping in our group,[23] and that of $LiNi_{0.3}Cu_{0.1}Fe_{0.2}Mn_{1.4}O_4$ reported here. To serve as a qualitative comparison, the current is normalized to the maximum value. Above 4.4 V, all characteristic peaks observed in undoped material are also observed in the doped material, even though the peak positions and their corresponding widths are not exactly the same. A slight difference is observed in the lower potential region. The CV curve of the doped material between 3.8 and 4.4 V shows a weak and very broad feature. Further inspection of this voltage region suggests that this feature consists of two overlapping peaks at around 4.08 and 4.21 V, resulting in an almost plateau-like crest (see the zoom in Figure 3a). The position of the first peak at 4.08 V is similar to the position of the redox couple Mn^{4+}/Mn^{3+} for the parent compound $LiNi_{0.4}Fe_{0.2}Mn_{1.4}O_4$ (see Figure 5b in ref 23). This peak is weak because most of the Mn in the calcined sample is already in the 4+ state (see the section about XPS analysis). The additional peak centered at 4.21 V for the doped material is most likely associated with the redox couple of Cu^{3+}/Cu^{2+}.[13] The activation of Cu is also supported by the conclusion from Raman spectroscopy that Cu has been successfully incorporated into the spinel phase after calcination. The peak positions in this voltage region are slightly different from the positions reported by Verrelli et al. for $Li_{0.85}Ni_{0.46}Cu_{0.1}Mn_{1.49}O_4$ material, which are at 4.02 V for Mn^{4+}/Mn^{3+} and 4.28 for Cu^{3+}/Cu^{2+}.[13] The difference in chemical composition might explain this slight deviation; the peak position and its shape are strongly affected by the local environment.[13] Additionally, these two peaks are very broad and strongly overlapping, making it difficult to determine precisely their peak positions.

Two intense peaks centered at 4.74 and 4.84 V are associated with the Ni^{4+}/Ni^{2+} redox couples.[23] A weak shoulder at around 5.0 V is located at the same position as the shoulder reported for the parent compound $LiNi_{0.4}Fe_{0.2}Mn_{1.4}O_4$.[23] Based on *in situ* Mössbauer spectroscopy and X-ray absorption spectroscopy analysis of the Fe-doped spinel material, Dräger et al. confirmed that this weak shoulder can be assigned to the Fe^{4+}/Fe^{3+} redox couple.[34]

The cycling stability and Coulombic efficiency for the calcined sample are displayed in Figure 3c,d, respectively. The capacity is measured with the charge/discharge rate of $C/2$. The charge capacity in the first cycle is larger than that in the following cycles (143 mAh g^{-1} in the first cycle vs 134 mAh g^{-1} in the second cycle). The Coulombic efficiency of the first cycle is only 90%, and it increases to 96% in the second cycle and reaches slightly above 98% from the 44th cycle onward. The capacity retention of this positive electrode is 89% (equivalent to 112 mAh g^{-1}) after 200 cycles, which is comparable to that observed without Cu doping.[23] The Li^+ incorporation might actually be facilitated by the truncated octahedral morphology. In addition, the presence of Mn^{3+} in the spinel resulting from oxygen loss at high calcination temperatures improves the electronic conductivity due to the electron hopping between Mn^{3+} and Mn^{4+}.[35] This is particularly advantageous for enhanced capacity retention.

To evaluate the rate capability of this material, the calcined $LiNi_{0.3}Cu_{0.1}Fe_{0.2}Mn_{1.4}O_4$ was charged by applying a constant current (at $C/2$) followed by a constant-voltage step at 5.3 V for 15 min, but then the electrodes were discharged with different rates. The rate-dependent discharge capacity is given in Figure 3e. The discharge capacity at the rate of 20C is equivalent to 62% capacity at the rate of $C/2$, which makes it a suitable candidate for high-power applications.

The reported material showed an initial specific discharge capacity of 126 mAh g^{-1} at a rate of $C/2$ in a voltage range between 3.5 and 5.3 V (vs Li^+/Li). The material exhibits a better capacity than those doped with Al,[10] Cu,[13] and Zr with a disordered LNMO structure,[15] but it is fairly similar to those doped with Na.[9]

It should be noted that the electrode mass loading used in this study is relatively low, 2.2 ± 0.4 mg cm^{-2}. It is anticipated that thicker electrodes will affect the electrochemical performance of this material as a positive electrode; in particular, the rate performance above 1C might be lower as reported here.

Surface Analysis by XPS. To shed more light onto the oxidation states at the surface of the positive electrode material, *ex situ* XPS was performed for positive electrodes at selected potentials. For all samples, Mn 2p, Mn 3s, Cu 2p, Ni 2p, O 1s, F 1s, and C 1s core-level spectra were recorded. The signal-to-noise ratio is low in the case of Ni 2p, Cu 2p, and Fe 2p spectra, caused by lower concentration of these elements in the electrode. Therefore, a reliable fitting method cannot be applied to these spectra to obtain the proper chemical states of these elements. Moreover, the oxidation state of these

https://dx.doi.org/10.1021/acsomega.0c02174
ACS Omega 2020, 5, 22861−22873

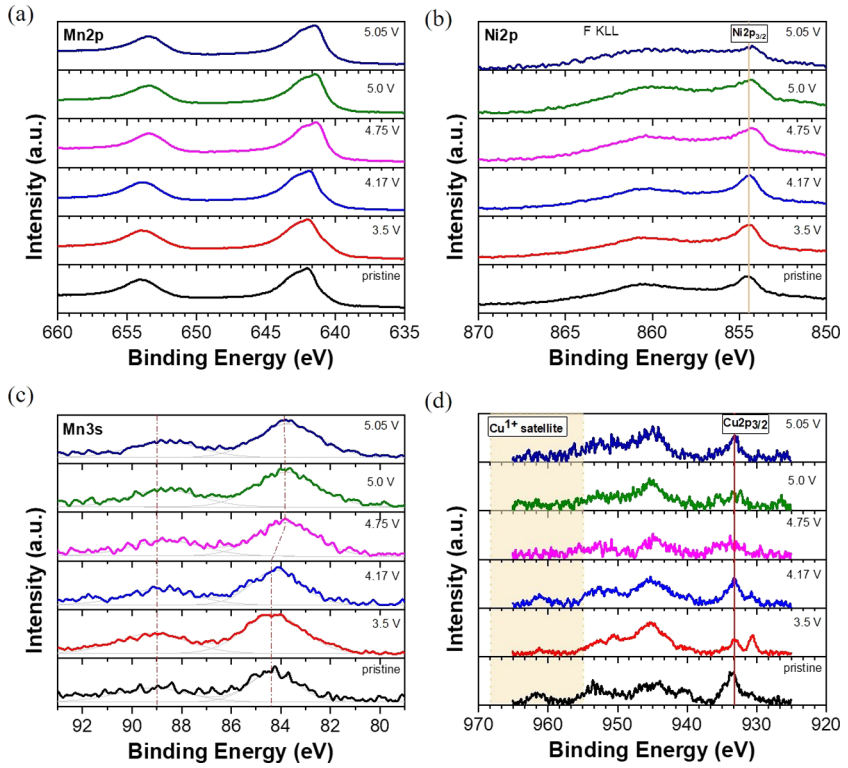

Figure 4. XPS spectra of (a) Mn 2p, (b) Ni 2p, (c) Mn 3s, and (d) Cu 2p of noncycled and precycled positive electrodes. For the samples at selected potentials, the positive electrodes were precycled with a rate of C/4 followed by the constant-voltage (holding time at selected potential for 24 h) step.

elements and their complex chemical nature, i.e., multiple doping material, make it more challenging to fit these spectra.

The Mn 2p and Ni $2p_{3/2}$ core-level spectra are shown in Figure 4a,b, respectively. It can be observed that there is no significant change in the shape and position of the Mn 2p peak at different potentials. Due to multiple possible oxidation states and overlapping of their binding energy, it is not straightforward to determine the oxidation state of Mn from Mn 2p core-level spectra.[36] The Ni 2p peak at 854.4 eV corresponds to the Ni $2p_{3/2}$ core-level spectra.[37−39] A broad peak close to Ni $2p_{3/2}$ is visible, which corresponds to the F KLL Auger peak. At the X-ray excitation energy of 1436.6 eV, which was used in this measurement, the strong overlapping between the broad F KLL Auger peak[40] (the F signal comes from the poly(vinylidene difluoride) (PVDF), used as a binder) and the weak Ni 2p peak increases the complexity of the analysis of Ni 2p to determine the oxidation states of Ni in the sample. Due to this complexity, the change of oxidation states of the Ni species at different potentials cannot be concluded for this particular material system.

Fortunately, the Mn 3s spectra can be used to determine the oxidation state of Mn species in this complex material system. In general, the Mn 3s core-level spectrum splits into two peaks due to the multiplet splitting. The oxidation state of Mn is characterized by the separation of these two peaks: the distance between these peaks changes from 4.5 eV for Mn^{4+} to 6.5 eV for Mn^{2+}.[41] In the case of the noncycled (pristine) electrode, the distance between the two Mn 3s peaks is about 4.8 eV, which corresponds to predominant Mn^{4+} states for the Mn species; however, the coexistence of a small amount of Mn^{3+} cannot be completely excluded. This confirms the successful strategy to improve the structural stability of a spinel by suppressing the amount of Mn^{3+}, which is a Jahn−Teller active ion. The Mn 3s core-level spectrum of the positive electrodes (Figure 4c) has two peaks separated by a distance ranging from 4.8 to 5.4 eV from each other. The distance between these peaks is an indication of different oxidation states for Mn.

The peak distances for pre-cycled positive electrodes at 3.5 and 4.172 V are the same, i.e., at around 4.8 eV, which means that the average oxidation state of Mn for the samples at these two potentials is 4+. The results are contradictory to the CV curves where the Mn is supposed to be at a more reduced state (Mn^{3+}) for the sample at 3.5 V. Note that the samples for the XPS measurements were precycled with a constant current for one cycle, followed by the constant-voltage step at 3.5 V for 24 h. This constant-voltage procedure might induce chemical instability for this sample. The Mn^{3+} is well known to undergo a disproportionation reaction, forming Mn^{2+} and Mn^{4+} where Mn^{2+} is dissolved into a carbonate-based electrolyte. This might explain that the average oxidation state for the sample at 3.5 V is 4+, rather than a more reduced state.

Manganese is expected to be electrochemically inactive above 4.2 V; hence, the Mn in samples at higher potential should have the same oxidation state as for the sample at 4.172 V. However, the peak distances for all of the samples above 4.2 V are 5.4 eV, which means that the Mn is actually in more reduced states than that of the sample at 4.172 V.[38] This unexpected result might be related to the side reaction(s), which are reported elsewhere for the oxide-based electrodes that have been cycled to higher potential. The decomposition products of both electrolyte and electrode are then deposited on the surface of the electrode.[42−44] Lin et al. reported that the reduced Mn and Co species are predominantly observed on

https://dx.doi.org/10.1021/acsomega.0c02174
ACS Omega 2020, 5, 22861−22873

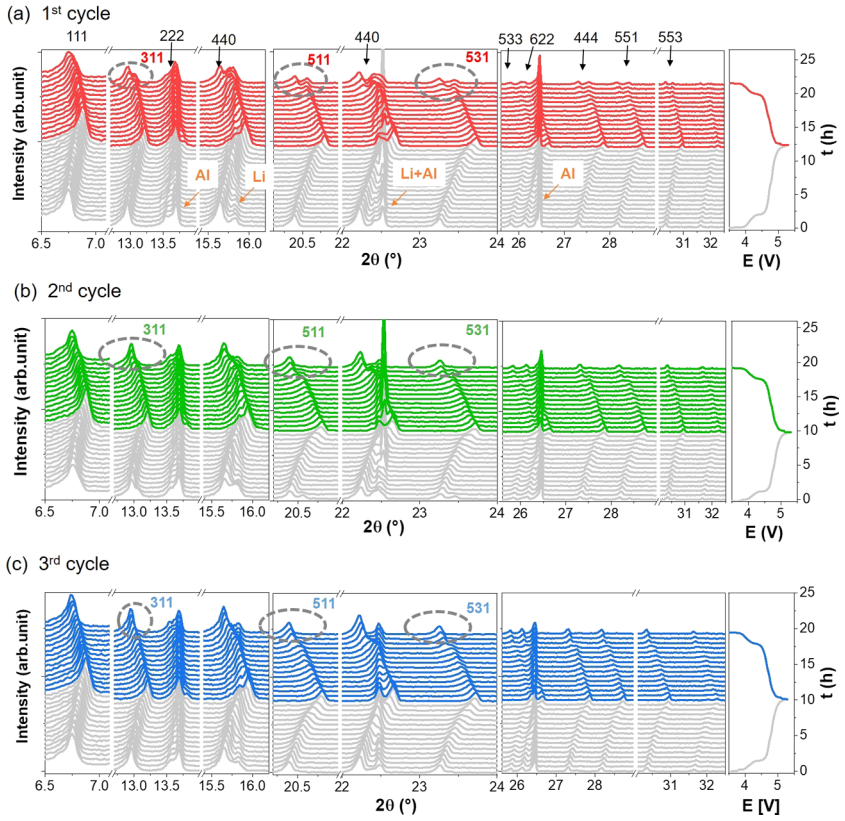

Figure 5. *In operando* X-ray diffraction patterns acquired during cycling of $LiNi_{0.3}Cu_{0.1}Fe_{0.2}Mn_{1.4}O_4$ vs Li at a rate of *C*/10 in the range of 3.5−5.3 V for (a) the first, (b) second, and (c) third cycles.

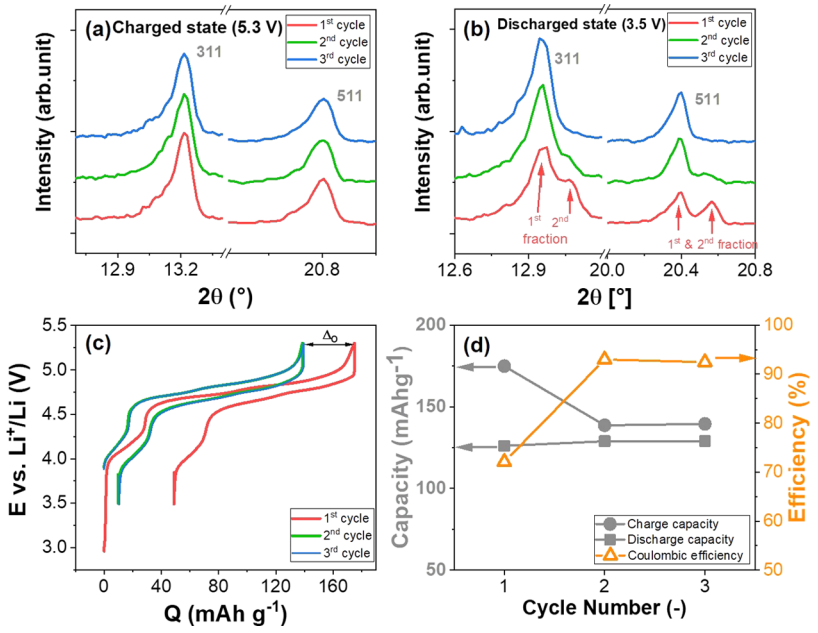

Figure 6. X-ray diffraction (XRD) patterns (a) at the end of charging at 5.3 V and (b) at the end of discharging at 3.5 V, (c) potential vs charge flow plot, and (d) capacity and Coulombic efficiency of the first, second, and third cycles during *in operando* XRD measurements.

the surface of $LiNi_{0.4}Mn_{0.4}Co_{0.18}Ti_{0.02}O_2$, cycled up to 4.7 V.[43] Since XPS is a surface-sensitive method, it is likely that the signals of Mn 3s for the samples above 4.2 V come predominantly from these decomposition products. The strong indication of side reactions can also be deduced from *in operando* XRD measurements.

The Cu 2p spectra are given in Figure 4d. The main peak at around 933.0 eV and a broad peak ranging from 942.0 to 948.0 eV are observed, corresponding to the Cu $2p_{3/2}$ and Cu satellite, respectively.[45] The broad and visible satellite peak at this position indicates that the oxidation state of Cu is 1+ for all samples.[45] This is unexpected because Cu is supposed to be at 2+ at 3.5 V and oxidized to 3+ above 4.21 V. Again, it

https://dx.doi.org/10.1021/acsomega.0c02174
ACS Omega 2020, 5, 22861−22873

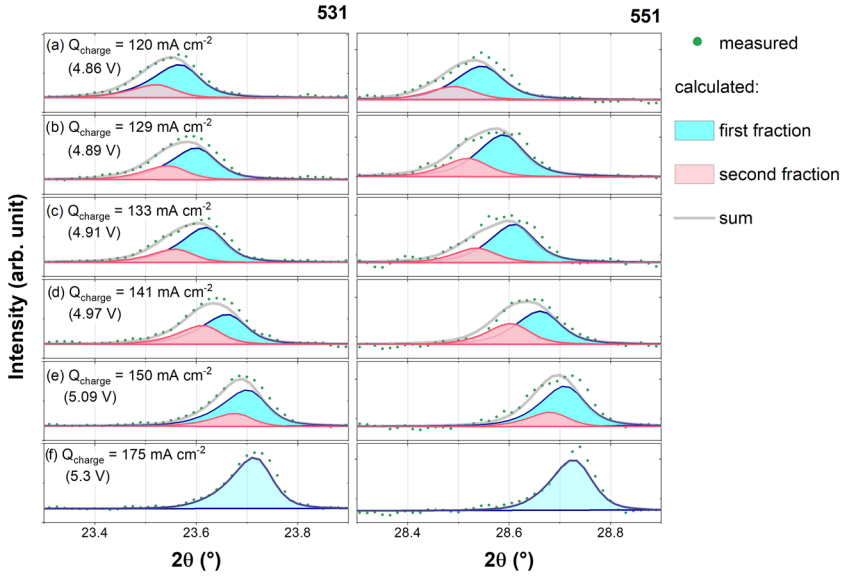

Figure 7. Measured and calculated 531 and 551 reflections at selected charge flows during the first charge. The corresponding voltages are given.

should be kept in mind that XPS is a surface-sensitive method; therefore, the results might not necessarily represent oxidation states of the elements in the bulk.

Mechanism of Lithium (De)intercalation and the Origin of Poor Coulombic Efficiency in the First Cycle. All electrochemical tests suggest that the (de)lithiation mechanism of the first cycle might not be the same as for the following cycles. For this reason, *in operando* XRD experiments were carried out during the first three cycles in the same voltage range as for the cycling stability test between 3.5 and 5.3 V (vs Li^+/Li). Considering that a reasonable acquisition time for *in operando* XRD patterns employing a silver source is 20 min/pattern, the cell was cycled with the charge rate of C/10 to get sufficient data points.

The *in operando* XRD patterns and their corresponding potential curves are presented in Figure 5a for the first, (b) second, and (c) third cycles. Due to the high background level originating from the separator, electrolyte, conductive agent (Super P), and binder (PVDF), the impurity phase of Li_2MnO_3 cannot be observed from these patterns. As it is seen in these figures, some reflections attributed to the positive electrode material, such as 222, 440, and 622, overlap with the reflections assigned to Li (as a counter electrode) or Al (as current collector) metals. On the other hand, the 311, 511 and 531 reflections do not overlap with reflections of either the counter electrode (Li) or the current collector (Al). Additionally, those reflections are observed at a medium 2θ range, which make them suitable reflections to be compared for qualitative analysis of the lithiation state at the same potential but at a different cycle number.

It is clear from Figure 5a–c that all positive electrode reflections shift to higher 2θ angles monotonically during charging (see the shift of gray patterns), which means that the lattice parameter decreases due to the extraction of lithium from the positive electrode. To evaluate the lithiation state at the end of charge at 5.3 V, the 311 and 511 reflections are presented for the first three cycles in Figure 6a. As seen in this figure, the peak positions of the 311 and 511 reflections are located at the same 2θ position, indicating that the positive electrode is essentially at the same lithiation state for the first, second, and third cycles, even though the exchanged charge of the second and third cycles is smaller than that of the first cycle. The difference between the charge capacity of the first and the second cycle is around 35 mAh g^{-1}, which is around 20% of the total capacity of the first charge. This difference is labeled as Δ_O in Figure 6c and is most likely used for the oxidative parasitic reaction in the first charge.

During discharging, all reflections shift gradually to lower 2θ angles (see the patterns in red, green, and blue in Figure 5); hence, the lattice parameter increases due to lithium intercalation into the positive electrode. However, the contraction and expansion of the lattice parameter is partially irreversible during the first cycle, indicated by overlapping contributions of doubling reflections at the end of discharge of the first cycle. This doubling of reflections is clearly visible in the case of 311, 511, and 531 reflections (see the dashed gray circles), but it is less obvious for other reflections because they overlap with reflections from either Li or Al. The doubling of reflections implies the coexistence of two spinels having different lithium contents; they are called the first and the second fraction of the spinel in this paper. With the current setup where the size of the X-ray beam (in the mm range) is considerably larger than the particle size of the positive electrode material (primary particle: hundreds of nanometers, secondary particle: few micrometers), it is not possible to locate precisely at which length scale this local inhomogeneity takes place, whether inside one primary particle or if it rather occurs in the secondary (agglomerated) particle.

The evolution of the 311 and 511 reflections at the end of discharge at 3.5 V is compared for the first three cycles in Figure 6b. Interestingly, the doubling of reflections gets less visible in the second cycle (relative to the first cycle) and it even disappears in the third cycle. The positions of those reflections are observed at similar 2θ angles, but the relative intensity between the first and the second fraction varies with the cycle number. The weight percentage of the first fraction increases in the second cycle, and it reaches a maximum in the third cycle. In other words, the positive electrode is not fully lithiated during discharging in the first cycle, but it becomes fully lithiated at the end of discharge in the third cycle.

To get a more quantitative and detailed understanding of the (de)lithiation mechanism, a Rietveld refinement was employed

https://dx.doi.org/10.1021/acsomega.0c02174
ACS Omega 2020, 5, 22861−22873

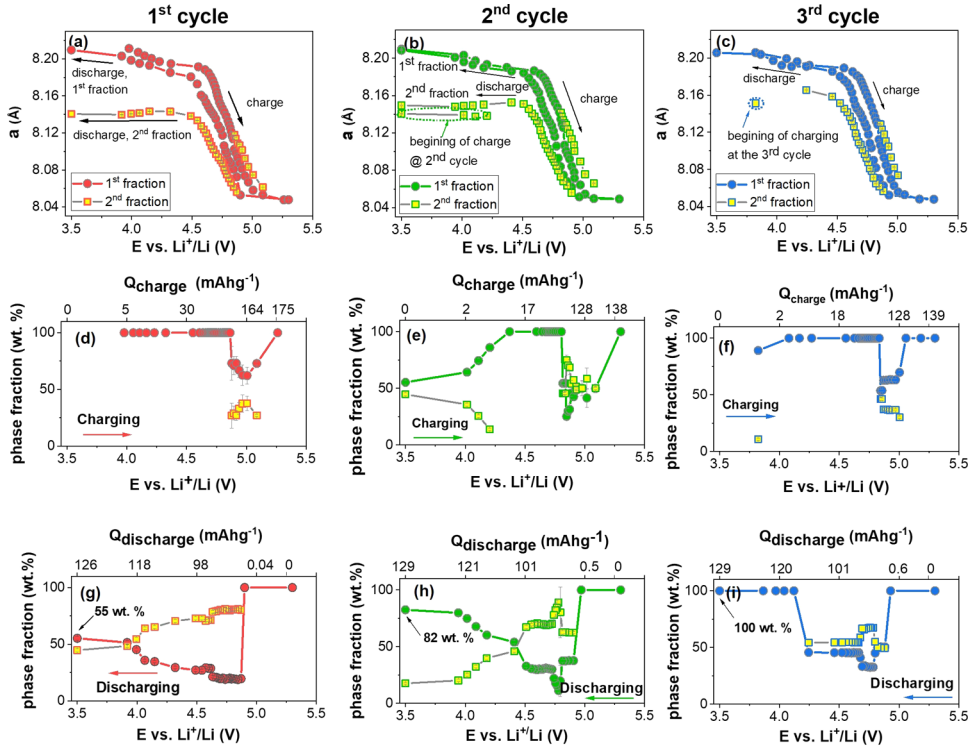

Figure 8. Evolution of the lattice parameter (a–c) and weight percentage of the first and the second fraction during charging (d–f) and discharging (g–i) of the first, second, and third cycles, respectively. The error bars from the refinement are not always visible because they are smaller than the size of the symbols.

for obtaining lattice parameter evolution. At the potential where the state of charge is locally not uniform, a structure model consisting of two spinel fractions of an identical space group having different lattice parameters is established. The aluminum current collector and the lithium metal negative electrode reflections were treated with the Le-Bail profile matching method.[46]

The coexistence of the first and the second fraction is not always observed as doubling of reflections as it is observed at the end of the first discharge in Figure 6b. In the voltage range between 4.86 and 5.09 V during the first charge, these two fractions are indicated from the peak shapes at higher angles (e.g., 531 and 551 reflections in Figure 7). The most pronounced indication is presented in Figure 7b–d where the 551 reflections exhibit plateau-like crests, resulting from strong overlapping of two peaks. A structure model based on heterogeneous lithium content in this voltage range improves the goodness-of-fit parameter (smaller χ value in FullProf). As it can be seen in this figure, the peak positions of the first and the second fraction shift continuously to a higher angle (shaded areas in blue and red). The integrated intensity of the second fraction becomes smaller as the charging continues.

The evolution of the lattice parameter as a function of voltage is presented in Figure 8a for the first, (b) second, and (c) third cycles. In the voltage region between 4.86 and 5.09 V, the lithium deintercalation is indicated by both the gradual decrease of the lattice parameter and the variation of the weight percentage of the two fractions. Two spinel fractions are also observed during discharging. Below 4.5 V, lithium intercalation leads to an increase of the lattice parameter and weight percentage of the first fraction. Opposite to this, the lattice parameter of the second fraction is practically constant, but its weight percentage gradually decreases (Figure 8g). At the end of the first discharge, only 55 wt % of the positive electrode is fully lithiated. The remaining 45 wt % of electrode material is partially lithiated. This of course raises the question on how the lithiation mechanism in this region proceeds, which is discussed below.

To get a more quantitative figure on the difference between the lithiation degree at the end of the first and the third cycle, a simplified estimation is made, based on the assumption that the lattice parameter varies linearly with the amount of lithium and that, while discharge capacities measured during the first and the second cycle comprise lithiation and parasitic reactions, the discharge capacity measured in the third cycle actually contributes to lithiation only. The lattice parameter of the first fraction of the positive electrode (55 wt %) at the end of the first discharge is at a fully lithiated state; however, as it is shown in Figure 9a, the lattice parameter of the remaining 45 wt % (red square) is identical with the lattice parameter that is observed when the state of lithiation at the third discharge is in the range of 46–70% (blue sphere or blue square). A more accurate estimation is not possible because two fractions of the spinel coexist within this range. Considering the two fractions, where one is only partially lithiated, this means that in total the average lithiation at the end of the first cycle is around 14–24% smaller than that of the third cycle.

Figure 9b presents a closer look into the discharge curves of the first and the third cycle. The discharge capacity of the first cycle is 2.8 mAh g^{-1} smaller (~2%) than that of the third cycle. This value is much smaller than the difference in lithiation degree estimated from XRD analysis. One possible explanation for this large discrepancy is the coexistence of reductive parasitic reactions, mostly occurring in the first and the second cycle. A considerable amount of discharge current of around 17–31 mAh g^{-1} is used for the parasitic reaction in the first

https://dx.doi.org/10.1021/acsomega.0c02174
ACS Omega 2020, 5, 22861–22873

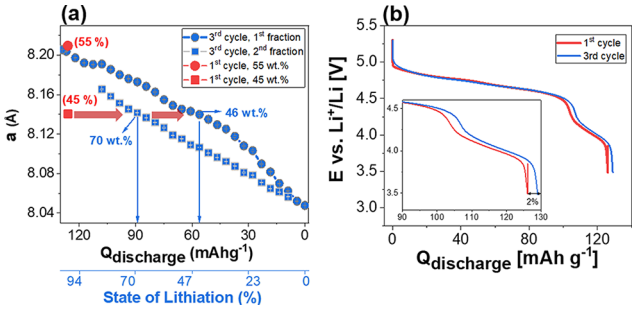

Figure 9. (a) Lattice parameter evolution as a function of discharge capacity in the third cycle. The corresponding state of lithiation shown below the figure is calculated based on the assumption that all discharge current is used for lithium intercalation. The lattice parameter at the end of the first discharge is also shown. (b) Discharge curves of the first and the third cycle during *in operando* XRD measurements.

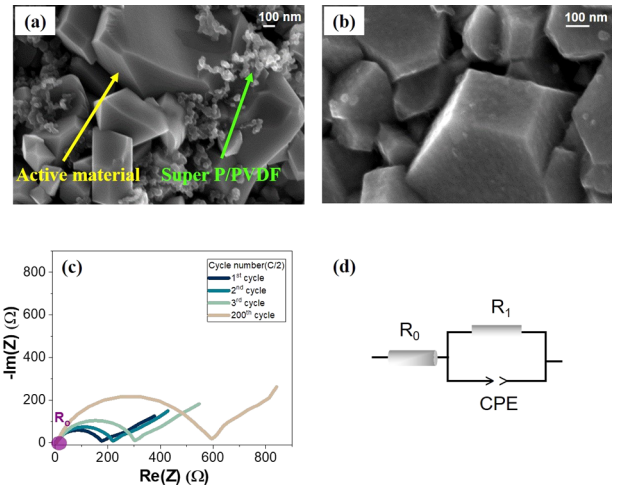

Figure 10. SEM images of electrodes (a) before cycling and (b) after 200 cycles with a cycling rate of $C/2$. (c) Nyquist plots of the positive electrodes at different cycle numbers. (d) Equivalent circuit model to fit the impedance spectra in (c).

cycle. Applying the same calculation, a discharge capacity of around 6−10 mAh g^{-1} is used for the parasitic reaction in the second cycle.

The coexistence of the two fractions of the spinel at the end of the first and the second charge might be misunderstood as a two-phase mechanism. However, *in operando* XRD analysis of the third cycle confirms that the lithiation in $LiNi_{0.3}Cu_{0.1}Fe_{0.2}Mn_{1.4}O_4$ follows a solid-solution mechanism. The possible explanation of the two fractions of the spinel at the end of the first and the second discharge is the coexistence of a reductive parasitic reaction, impeding the lithiation process. The solid-solution mechanism is further confirmed by the results of *in operando* XRD conducted between 3.5 and 5.1 V where only one fully lithiated spinel phase is observed already at the end of the first discharge. The *in operando* XRD patterns, the evolution of the lattice parameter, and the voltage profiles are presented in Figures S4 and S5 in the Supporting Information.

To further investigate the influence of current on the parasitic reactions, another *in operando* XRD experiment was carried out between 3.5 and 5.3 V for four cycles with rates of $C/10$, $C/10$, $C/30$, and $C/10$. The *in operando* XRD patterns of the first and the second cycle are the same as in Figure 5a,b; therefore, only the patterns of the third and the fourth cycle ($C/30$, then $C/10$) are given in Figure S6a,b, respectively. Even though a significant amount of capacity of 148 mAh g^{-1} is measured from 5.08 to 5.3 V during charging at a rate of $C/30$, the positions of all reflections attributed to the positive electrode material do not shift any longer in this range, which indicates that this additionally measured charge is not used for further lithium extraction from the positive electrode. This last set of *in operando* XRD experiments suggests that the use of low rates at high voltages considerably promotes side reactions, which detrimentally affects the cycling performance of the positive electrode.

The side reaction influences greatly the capacity retention of the positive electrode by consuming lithium and through formation of a surface reconstruction layer, which increases the overall impedance, leading to capacity and power loss. The change of morphology and impedance due to cycling is likely and investigated by performing SEM and impedance spectroscopy. Figure 10a,b shows the morphology of active material in the positive electrode before cycling and after 200 cycles. It is visible that the surface of the active material gets rougher after 200 cycles. Some of the decomposition products might be deposited at the surface, worsening the kinetics of the electrochemical process.

The impedance spectra of the positive electrode at 4.65 V (corresponding to the state of charge of 20% at the beginning of life) are presented as Nyquist plots in Figure 10c for different cycle numbers. It is shown here that the general features are preserved during prolonged cycling up to 200 cycles. They consist of a nearly straight line of a diffusional tail (Warburg impedance) at a lower frequency range, followed by a depressed semicircle at a medium- to high-frequency range. The impedance value at $-Im(z)$ equal to zero (R_0), observed in the high-frequency region, represents the pure Ohmic resistance of all components in the cell such as electrolyte, binder and separator.[47] The depressed arc is most likely associated with the charge transfer resistance at the positive electrode side. Even though the formation of a surface reconstruction layer is reported elsewhere,[42−44] and also indicated in this study, only one semi-circle is observed. This is opposite to the impedance spectra of a graphite negative electrode where the resistance of the solid electrolyte interphase and charge transfer can be clearly identified from two suppressed arcs at higher- and medium-frequency ranges.[48] It is possible that the resistance of this surface reconstruction layer at the positive electrode side is strongly overlapping with the charge transfer resistance and has a very small value compared to the charge transfer resistance so that the depressed arc is dominated by the charge transfer resistance.

The equivalent circuit, consisting of an R_0 and an RQ element (see Figure 10d), is used to fit the impedance spectra. The Warburg impedance is not considered in this fitting. The diffusional tail is actually overlapping with another process, resulting in a nonlinear tail, which is most obvious for the spectra in the 200th cycle. The RQ element consists of charge transfer resistance (R_1) in parallel with the constant-phase element (CPE). Stiaszny et al. suggested to use CPE, instead of pure capacitance, because it can well describe the porous electrode.[48] The fitted R_0 and R_1 values are listed in Table 2. It is seen in this table that both resistances, R_0 and R_1, increase

https://dx.doi.org/10.1021/acsomega.0c02174
ACS Omega 2020, 5, 22861−22873

Table 2. Values of Fitted R_0 and R_1

cycle number	R_0 (Ω)	R_1 (Ω)
1	1.7 (±0.07)	178 (±3)
2	2.0 (±0.1)	225 (±4)
3	2.2 (±0.13)	316 (±6)
200	5.1 (±0.13)	594 (±8)

due to cycling. This increase of impedance causes a sluggish electrochemical reaction at higher cycle numbers.

SUMMARY AND CONCLUSIONS

$LiNi_{0.3}Cu_{0.1}Fe_{0.2}Mn_{1.4}O_4$ with an $Fd\bar{3}m$ structure has successfully been synthesized via a sol−gel method and subsequent calcination at 850 °C. The stabilization of the structure could be attributed to the increased disorder due to multiple-cation incorporation. The electrochemical performance depends on various factors such as cation disordering, particle size and shape, and the presence of Mn^{3+} and Cu^{2+}. A detailed analysis of the *in operando* XRD data reveals that Li^+ insertion/extraction occurs via a solid-solution process. The appearance of a secondary spinel domain during cycling can be explained by a non-uniform lithium content across the positive electrode, leading to a local variation of the state of charge. With the co-doping of Cu and Fe in the LNMO system, no significant improvements in the specific capacity as compared to the literature could be attained. Nevertheless, the disordered spinel structure could be obtained at a lower calcination temperature of 850 °C, in comparison to its parent compound without Cu doping $LiNi_{0.4}Fe_{0.2}Mn_{1.4}O_4$ (at 1000 °C). Therefore, depending on the choice of dopants and the synthesis route, multication doping can be considered as an attractive strategy to stabilize the $Fd\bar{3}m$ structure and enhance the electrochemical properties in high-voltage spinels. Employing rate-dependent *in operando* XRD measurements, it is concluded that side reactions occur predominantly during charging and discharging of the first cycle. The XPS results suggest that the surface reconstruction layer, formed due to these side reactions, consists of species that are in more reduced states than in the bulk. Fortunately, this layer protects the positive electrode surface and suppresses the side reaction during successive cycles. The studies conducted here suggest that the relevant parameters to control the side reaction are charge/discharge rate and operating voltage. The use of a higher cycling rate and decreasing the upper limit of the voltage window might suppress the side reactions.

EXPERIMENTAL SECTION

Synthesis. Stoichiometric amounts of metal acetates, viz., manganese(II) acetate tetrahydrate (Merck Millipore, ≥99%), lithium acetate dihydrate (Alfa Aesar, 99%), iron(II) acetate anhydrous (Alfa Aesar), nickel(II) acetate tetrahydrate (Alfa Aesar, >98%), and copper(II) acetate monohydrate (Alfa Aesar, >98%), were dissolved in a solution of 1:4 citric acid monohydrate (EMSURE, ≥99.5%) and ethylene glycol (AnalaR NORMAPUR, ≥99.5%). The homogeneous solution was then heated to 180 °C to remove excess ethylene glycol. The viscous gel thus formed was dried at 400 °C for 5 h in a muffle furnace. The obtained material was then calcined with a rate of 5 °C min^{-1} in air. In respect to the electrochemical performance of the synthesized materials, the optimum calcination temperature was found to be 850 °C. The electrochemical performance of samples at different calcination temperatures are given in Figure S1 in the Supporting Information. The sample for *in operando* measurements was synthesized in a similar way, except that the molar ratio of citric acid monohydrate to ethylene glycol was 1:8 to ensure better homogenization.

Material and Electrochemical Characterization. The metal compositions of the calcined samples were measured by inductively coupled plasma optical emission spectrometry (ICP-OES, iCAP 7600 from Thermo Fisher Scientific). For this measurement, the sample was dissolved in hydrochloric acid and nitric acid at 353 K in a graphite oven (Analab). Four different calibration solutions and two internal standards (sodium and scandium) were used to perform the elemental analysis. The oxygen content was determined by carrier gas hot extraction (CGHE).

X-ray diffraction (XRD) experiments were conducted on the as-prepared powder samples for phase analysis (STOE STADI/P diffractometer in transmission geometry, Cu $K\alpha_1$ radiation, Ge 111 monochromator, Mythen 1D silicon strip detector). The samples were scanned from 4 to 100 ° (2θ). Structural refinements were carried out by the Rietveld method using the FullProf software.[24] The instrumental resolution function was determined from the reflections' half widths from a Si standard (NIST 640d) pattern. Further confirmation of the crystal structure of the spinel was done by recording Raman spectra at room temperature on a HORIBA Jobin Yvon LabRAM HR Evol system with 632.81 nm laser excitation. ^{7}Li magic-angle spinning nuclear magnetic resonance (MAS NMR) spectroscopy was conducted on a Bruker Avance 200 MHz system at a magnetic field of B_0 = 4.7 T, which corresponds to a ^{7}Li Larmor frequency ν_L = 77.8 MHz. An aqueous solution of 1 M LiCl was taken as a reference for the chemical shift of ^{7}Li (0 ppm). Spinning was performed in 1.3 mm rotors at 40 kHz. Spectra were recorded with a rotor-synchronized Hahn-echo pulse sequence, a $\pi/2$ pulse length of 1 μs, and a recycle delay of 1 s.

The morphologies of the as-synthesized powder and electrodes were investigated by thermal field emission (FE) scanning electron microscopy (SEM), using a ZEISS Merlin scanning electron microscope (5 kV, in-lens detector). Prior to the SEM measurements, all samples were sputtered with Au/Pd (Au = 80% and Pd = 20%) with a thickness of 5 nm to reduce charging effects.

The electrodes for electrochemical measurements, as well as for *in operando* XRD measurements, were prepared by a magnetically stirred (24 h, room temperature) mixture of 80 wt % active material, 10 wt % carbon (Super C 65, TIMCAL), and 10 wt % poly(vinylidene fluoride) (Solef PVDF 6020 binder, Solvay) dissolved in *N*-methyl-2-pyrrolidone (NMP, Sigma-Aldrich), where the weight ratio of NMP and the total solid content was 2:1. The obtained slurry was coated on an aluminum foil by a doctor blade method with a wet thickness of 150 μm for electrochemical measurements and 500 μm for *in operando* XRD. The dried coatings were punched with a diameter of 1.2 cm to form electrode disks. The mass loading of electrodes was 2.2 ± 0.4 mg cm^{-2} for electrochemical tests and 8.8 mg cm^{-2} for *in operando* XRD measurements. The electrochemical characterization was conducted in a half-cell configuration using CR2032-type coin cells. $LiPF_6$ (1 M) in ethylene carbonate (EC)/dimethyl carbonate (DMC) (1:1, v/v) electrolyte (LP30, Merck) in excess and two layers of Celgard 2325 as a separator were utilized for building the cells. Lithium metal was used as a counter electrode.

https://dx.doi.org/10.1021/acsomega.0c02174
ACS Omega 2020, 5, 22861−22873

All of the electrochemical measurements were performed at room temperature. The cells were tested with a BCS (Bio-Logic Science Instruments) multichannel potentiostat using the EC-Lab software. The cells were cycled between 3.5 and 5.3 V. The relatively high upper cutoff voltage (5.3 V) was used to ensure the iron redox activity. Cycling performances were investigated by cycling the cells at a rate of $C/2$ (where 1C = 146.7 mA g^{-1}, the theoretical capacity of the current material) for 200 cycles with the electrolyte in excess. For rate capability investigations, a constant charging rate of $C/2$ followed by a constant-voltage step at 5.3 V for 15 min was employed, whereas discharging rates were varied as $C/2$, 1C, 5C, 10C, and 20C. For all electrochemical tests, a relaxation time at the end of charge and discharge was applied for 15 min. Cyclic voltammograms were measured with a sweep rate of 0.1 mV s^{-1}. To ensure reproducible results, at least two samples were cycled for each type of experiment.

***In Operando* XRD Measurements Using Ag Diffractometer.** *In operando* XRD measurements were performed using a dedicated *in operando* setup, developed at the Karlsruhe Institute of Technology in close cooperation with the STOE & Cie GmbH as presented in Figure S2 in the Supporting Information. The diffractometer has a silver source (E = 22.123 keV, λ = 0.55942 Å) with a focusing Ge 111 monochromator. A Dectris MYTHEN 2 2K double detector with a fixed distance between both detectors of little less than the width of a module (approximately 18° 2θ) is mounted at a radius of 130 mm from the central axis of the goniometer, enabling a simultaneous intensity counting covering the angular range from 0 to 36° with the effective angular resolution of 0.015° in 2θ. If necessary, the step width could be improved to 0.005° by an oversampling routine, which also increases the measuring time by a factor of 3. The electrochemical tests with *in operando* cells were accomplished using a galvanostatic system μAUTOLAB-FRA2, TYPE III controlled by NOVA. The cell was cycled at a rate of $C/10$ between 3.5 and 5.3 V for three cycles. The acquisition time was 20 min per pattern. Additional *in operando* XRD experiments were carried out to study the influences of cycling rate and voltage window on the lithium intercalation.

Prior to the *in operando* measurements, LaB_6 (NIST 660b) was used as a standard to determine the instrumental resolution file for the Rietveld refinement of the samples.

***Ex Situ* X-ray Photoelectron Spectroscopy (XPS).** For *ex situ* XPS measurements, the positive electrodes were galvanostatically precycled for one cycle with a constant rate of $C/4$. The positive electrodes were then charged to selected potentials using a constant-current ($C/4$)−constant-voltage mode for 24 h. The cells were opened under an argon atmosphere, and the samples were rinsed with DMC. All samples were transferred to the XPS instrument without any air contact. The measurements were carried out using a K-Alpha XP spectrometer (Thermo Fisher Scientific). The samples were excited with monochromatic an Al Kα X-ray source, and the analysis spot was 400 μm. Data acquisition and processing were done using the Thermo Avantage software.

Electrochemical Impedance Spectroscopy (EIS). EIS was carried out by introducing sinusoidal voltage signals of 5 mV using a multichannel potentiostat (BioLogic VMP3) in the frequency range of 1 MHz−1 mHz. The impedance data is evaluated using the RelaxIS software.

■ ASSOCIATED CONTENT

Supporting Information

The Supporting Information is available free of charge at https://pubs.acs.org/doi/10.1021/acsomega.0c02174.

Electrochemical performances of $LiNi_{0.3}Cu_{0.1}Fe_{0.2}Mn_{1.4}O_4$ at different calcination temperatures (Figure S1); *in operando* XRD experimental setup on Ag diffractometer (Figure S2); Raman mapping of uncalcined and calcined samples at 850 °C (Figure S3); *in operando* X-ray diffraction patterns during cycling of $LiNi_{0.3}Cu_{0.1}Fe_{0.2}Mn_{1.4}O_4$ vs Li between 3.5 and 5.1 V at a rate of $C/10$ (Figure S4); comparison of the 311 and 511 reflections at the end of charging and at the end of discharging for the cells cycled between 3.5−5.3 and 3.5−5.1 (Figure S5); XRD patterns of $LiNi_{0.3}Cu_{0.1}Fe_{0.2}Mn_{1.4}O_4$ vs Li at rates of $C/30$ and $C/10$ (Figure S6) (PDF)

■ AUTHOR INFORMATION

Corresponding Author

Mariyam Susana Dewi Darma − *Institute for Applied Materials (IAM), Karlsruhe Institute of Technology (KIT), 76344 Eggenstein-Leopoldshafen, Germany; Helmholtz Institute Ulm (HIU) Electrochemical Energy Storage, 89081 Ulm, Germany;* orcid.org/0000-0003-3853-3702; Email: mariyam.darma@kit.edu

Authors

Priyanka Sharma − *Institute for Applied Materials (IAM), Karlsruhe Institute of Technology (KIT), 76344 Eggenstein-Leopoldshafen, Germany*

Chittaranjan Das − *Institute for Applied Materials (IAM), Karlsruhe Institute of Technology (KIT), 76344 Eggenstein-Leopoldshafen, Germany*

Sylvio Indris − *Institute for Applied Materials (IAM), Karlsruhe Institute of Technology (KIT), 76344 Eggenstein-Leopoldshafen, Germany;* orcid.org/0000-0002-5100-113X

Thomas Bergfeldt − *Institute for Applied Materials (IAM), Karlsruhe Institute of Technology (KIT), 76344 Eggenstein-Leopoldshafen, Germany*

Liuda Mereacre − *Institute for Applied Materials (IAM), Karlsruhe Institute of Technology (KIT), 76344 Eggenstein-Leopoldshafen, Germany*

Michael Knapp − *Institute for Applied Materials (IAM), Karlsruhe Institute of Technology (KIT), 76344 Eggenstein-Leopoldshafen, Germany; Helmholtz Institute Ulm (HIU) Electrochemical Energy Storage, 89081 Ulm, Germany*

Udo Geckle − *Institute for Applied Materials (IAM), Karlsruhe Institute of Technology (KIT), 76344 Eggenstein-Leopoldshafen, Germany*

Helmut Ehrenberg − *Institute for Applied Materials (IAM), Karlsruhe Institute of Technology (KIT), 76344 Eggenstein-Leopoldshafen, Germany; Helmholtz Institute Ulm (HIU) Electrochemical Energy Storage, 89081 Ulm, Germany;* orcid.org/0000-0002-5134-7130

Complete contact information is available at: https://pubs.acs.org/10.1021/acsomega.0c02174

Notes

The authors declare no competing financial interest.

https://dx.doi.org/10.1021/acsomega.0c02174
ACS Omega 2020, 5, 22861−22873

■ ACKNOWLEDGMENTS

This work contributes to the research performed at CELEST (the Center for Electrochemical Energy Storage Ulm-Karlsruhe). The ICP-OES measurements were carried out with the support of the Karlsruhe Nano Micro Facility, a Helmholtz research infrastructure at the Karlsruhe Institute of Technology (KIT).

■ REFERENCES

(1) Jang, D. H.; Shin, Y. J.; Oh, S. M. Dissolution of Spinel Oxides and Capacity Losses in 4 V $Li/Li_xMn_2O_4$ Cells. *J. Electrochem. Soc.* **1996**, *143*, 2204−2211.

(2) Zhong, Q.; Bonakdarpour, A.; Zhang, M.; Gao, Y.; Dahn, J. R. Synthesis and Electrochemistry of $LiNi_xMn_{2-x}O_4$. *J. Electrochem. Soc.* **1997**, *144*, 205−213.

(3) Chi, L. H.; Dinh, N. N.; Brutti, S.; Scrosati, B. Synthesis, characterization and electrochemical properties of 4.8 V $Li-Ni_{0.5}Mn_{1.5}O_4$ cathode material in lithium-ion batteries. *Electrochim. Acta* **2010**, *55*, 5110−5116.

(4) Santhanam, R.; Rambabu, B. Research progress in high voltage spinel $LiNi_{0.5}Mn_{1.5}O_4$ material. *J. Power Sources* **2010**, *195*, 5442−5451.

(5) Yi, T.-F.; Fang, Z.-K.; Xie, Y.; Zhu, Y.-R.; Zang, L.-Y. Synthesis of $LiNi_{0.5}Mn_{1.5}O_4$ cathode with excellent fast charge-discharge performance for lithium-ion battery. *Electrochim. Acta* **2014**, *147*, 250−256.

(6) Yi, T.-F.; Li, Y.-M.; Li, X.-Y.; Pan, J.-J.; Zhang, Q.; Zhu, Y.-R. Enhanced electrochemical property of $FePO_4$-coated $LiNi_{0.5}Mn_{1.5}O_4$ as cathode materials for Li-ion battery. *Sci. Bull.* **2017**, *62*, 1004−1010.

(7) Lee, J.; Kim, C.; Kang, B. High electrochemical performance of high-voltage $LiNi_{0.5}Mn_{1.5}O_4$ by decoupling the Ni/Mn disordering from the presence of Mn^{3+} ions. *NPG Asia Mater.* **2015**, *7*, No. e211.

(8) Bhaskar, A.; Mikhailova, D.; Kiziltas-Yavuz, N.; Nikolowski, K.; Oswald, S.; Bramnik, N. N.; Ehrenberg, H. 3d-Transition Metal Doped Spinels as High-Voltage Cathode Materials for Rechargeable Lithium-Ion Batteries. *Prog. Solid State Chem.* **2014**, *42*, 128−148.

(9) Wang, J.; Lin, W.; Wu, B.; Zhao, J. Syntheses and electrochemical properties of the Na-doped $LiNi_{0.5}Mn_{1.5}O_4$ cathode materials for lithium-ion batteries. *Electrochim. Acta* **2014**, *145*, 245−253.

(10) Liu, G.; Sun, H.; Kong, X.; Li, Y.; Wang, B. Facile synthesis of high performance $LiNi_{0.5}Mn_{1.4}Mg_{0.1}O_4$ and $LiNi_{0.5}Mn_{1.4}Al_{0.1}O_4$ by a low temperature solution combustion synthesis method. *Int. J. Electrochem. Sci.* **2015**, *10*, 6651−6662.

(11) Aklalouch, M.; Amarilla, J. M.; Saadoune, I.; Rojo, J. M. $LiCr_{0.2}Ni_{0.4}Mn_{1.4}O_4$ spinels exhibiting huge rate capability at 25 and 55 °C: Analysis of the effect of the particle size. *J. Power Sources* **2011**, *196*, 10222−10227.

(12) Liu, J.; Manthiram, A. Understanding the Improved Electrochemical Performances of Fe-Substituted 5 V Spinel Cathode $LiMn_{1.5}Ni_{0.5}O_4$. *J. Phys. Chem. C* **2009**, *113*, 15073−15079.

(13) Verrelli, R.; Scrosati, B.; Sun, Y.-K.; Hassoun, J. Stable, High Voltage $Li_{0.85}Ni0._{46}Cu_{0.1}Mn_{1.49}O_4$ Spinel Cathode in a Lithium-Ion Battery Using a Conversion-Type CuO Anode. *ACS Appl. Mater. Interfaces* **2014**, *6*, 5206−5211.

(14) Mo, M.; Hui, K. S.; Hong, X.; Guo, J.; Ye, C.; Li, A.; Hud, N.; Huang, Z.; Jiang, J.; Liang, J.; Chen, H. Improved cycling and rate performance of Sm-doped $LiNi_{0.5}Mn_{1.5}O_4$ cathode materials for 5 V lithium ion batteries. *Appl. Surf. Sci.* **2014**, *290*, 412−418.

(15) Feng, S.; Kong, X.; Sun, H.; Wang, B.; Luo, T.; Liu, G. Effect of Zr doping on $LiNi_{0.5}Mn_{1.5}O_4$ with ordered or disordered structures. *J. Alloys Compd.* **2018**, *749*, 1009−1018.

(16) Yi, T.-F.; Xie, Y.; Zhu, Y.-R.; Zhu, R.-S.; Ye, M.-F. High rate micron-sized niobium-doped $LiMn_{1.5}Ni_{0.5}O_4$ as ultra high power positive-electrode material for lithium-ion batteries. *J. Power Sources* **2012**, *211*, 59−65.

(17) Yi, T.-F.; Chen, B.; Zhu, Y.-R.; Li, X.-Y.; Zhu, R.-S. Enhanced rate performance of molybdenum-doped spinel $LiNi_{0.5}Mn_{1.5}O_4$ cathode materials for lithium ion battery. *J. Power Sources* **2014**, *247*, 778−785.

(18) Sun, Y.-K.; Oh, S. W.; Yoon, C. S.; Bang, H. J.; Prakash, J. Effect of sulfur and nickel doping on morphology and electrochemical performance of $LiNi_{0.5}Mn_{1.5}O_{4-x}S_x$ spinel material in 3-V region. *J. Power Sources* **2006**, *161*, 19−26.

(19) Deng, Y.-F.; Zhao, S.-X.; Xu, Y.-H.; Gao, K.; Nan, C.-W. Impact of P-doped in spinel $LiNi_{0.5}Mn_{1.5}O_4$ on degree of disorder, grain morphology, and electrochemical performance. *Chem. Mater.* **2015**, *27*, 7734−7742.

(20) Li, J.; Li, S.; Xu, S.; Huang, S.; Zhu, J. Synthesis and Electrochemical Properties of $LiNi_{0.5}Mn_{1.5}O_4$ Cathode Materials with Cr^{3+} and F^- Composite Doping for Lithium-Ion Batteries. *Nanoscale Res. Lett.* **2017**, *12*, No. 414.

(21) Zhong, G. B.; Wang, Y. Y.; Yu, Y. Q.; Chen, C. H. Electrochemical investigations of the $LiNi_{0.45}M_{0.10}Mn_{1.45}O_4$ (M = Fe, Co, Cr) 5 V cathode materials for lithium ion batteries. *J. Power Sources* **2012**, *205*, 385−393.

(22) Shin, D. W.; Bridges, C. A.; Huq, A.; Paranthaman, M. P.; Manthiram, A. Role of Cation Ordering and Surface Segregation in High-Voltage Spinel $LiMn_{1.5}Ni_{0.5-x}M_xO_4$ (M = Cr, Fe, and Ga) Cathodes for Lithium-Ion Batteries. *Chem. Mater.* **2012**, *24*, 3720−3731.

(23) Yavuz, M.; Kiziltas-Yavuz, N.; Bhaskar, A.; Scheuermann, M.; Indris, S.; Fauth, F.; Knapp, M.; Ehrenberg, H. Influence of Iron on the Structural Evolution of $LiNi_{0.4}Fe_{0.2}Mn_{1.4}O_4$ during Electrochemical Cycling Investigated by in situ Powder Diffraction and Spectroscopic Methods. *Z. Anorg. Allg. Chem.* **2014**, *640*, 3118−3126.

(24) Rodríguez-Carvajal, J. Recent advances in magnetic structure determination by neutron powder diffraction. *Phys. B: Condens. Matter* **1993**, *192*, 55−69.

(25) Liu, H.; Wang, J.; Zhang, X.; Zhou, D.; Qi, X.; Qiu, B.; Fang, J.; Kloepsch, R.; Schumacher, G.; Liu, Z.; Li, J. Morphological Evolution of High-Voltage Spinel $LiNi_{0.5}Mn_{1.5}O_4$ Cathode Materials for Lithium-Ion Batteries: The Critical Effects of Surface Orientations and Particle Size. *ACS Appl. Mater. Interfaces* **2016**, *8*, 4661−4675.

(26) Höweling, A.; Stoll, A.; Schmidt, D. O.; Geßwein, H.; Simon, U.; Binder, J. R. Influence of Synthesis, Dopants and Cycling Conditions on the Cycling Stability of Doped $LiNi_{0.5}Mn_{1.5}O_4$ Spinels. *J. Electrochem. Soc.* **2017**, *164*, A6349−A6358.

(27) Miara, L.; Windmüller, A.; Tsai, C.-L.; Richards, W. D.; Ma, Q.; Uhlenbruck, S.; Guillon, O.; Ceder, G. About the Compatibility between High Voltage Spinel Cathode Materials and Solid Oxide Electrolytes as a Function of Temperature. *ACS Appl. Mater. Interfaces* **2016**, *8*, 26842−26850.

(28) Liu, J.; Li, G.; Yu, Y.; Bai, H.; Shao, M.; Guo, J.; Su, C.; Liu, X.; Bai, W. Synthesis and electrochemical performance evaluations of polyhedral spinel $LiAl_xMn_{2-x}O_4$($x \leq 0.20$) cathode materials prepared by a solution combustion technique. *J. Alloys Compd.* **2017**, *728*, 1315−1328.

(29) Sarkar, A.; Velasco, L.; Wang, D.; Wang, Q.; Talasila, G.; de Biasi, L.; Kübel, C.; Brezesinski, T.; Bhattacharya, S. S.; Hahn, H.; Breitung, B. High entropy oxides for reversible energy storage. *Nat. Commun.* **2018**, *9*, No. 3400.

(30) Samarasingha, P. B.; Andersen, N. H.; Sørby, M. H.; Kumar, S.; Nilsen, O.; Fjellvåg, H. Neutron diffraction and Raman analysis of $LiMn_{1.5}Ni_{0.5}O_4$ spinel type oxides for use as lithium ion battery cathode and their capacity enhancements. *Solid State Ionics* **2016**, *284*, 28−36.

(31) Amin, R.; Belharouk, I. Part I: Electronic and ionic transport properties of the ordered and disordered $LiNi_{0.5}Mn_{1.5}O_4$ spinel cathode. *J. Power Sources* **2017**, *348*, 311−317.

(32) Akgul, F. A.; Akgul, G.; Yildirim, N.; Unalan, H. E.; Turan, R. Influence of Thermal Annealing on Microstructural, Morphological, Optical Properties and Surface Electronic Structure of Copper Oxide Thin Films. *Mater. Chem. Phys.* **2014**, *147*, 987−995.

(33) Yu, D. Y. W.; Yanagida, K. Structural Analysis of Li_2MnO_3 and Related Li-Mn-O Materials. *J. Electrochem. Soc.* **2011**, *158*, A1015−A1022.

https://dx.doi.org/10.1021/acsomega.0c02174
ACS Omega 2020, 5, 22861−22873

(34) Dräger, C.; Sigel, F.; Witte, R.; Kruk, R.; Pfaffmann, L.; Mangold, S.; Mereacre, V.; Knapp, M.; Ehrenberg, H.; Indris, S. Observation of Electrochemically Active Fe^{3+}/Fe^{4+} in $Li-Co_{0.8}Fe_{0.2}MnO_4$ by In situ Mössbauer Spectroscopy and X-ray Absorption Spectroscopy. *Phys. Chem. Chem. Phys.* **2019**, *21*, 89−95.
(35) Kunduraci, M.; Amatucci, G. G. Synthesis and Characterization of Nanostructured 4.7 V $LixMn_{1.5}Ni_{0.5}O_4$ Spinels for High-Power Lithium-Ion Batteries. *J. Electrochem. Soc.* **2006**, *153*, A1345−A1352.
(36) Biesinger, M. C.; Payne, B. P.; Grosvenor, A. P.; Lau, L. W. M.; Gerson, A. R.; Smart, R. St. C. Resolving Surface Chemical States in XPS analysis of First Row Transition Metals, Oxides and Hydroxides: Cr, Mn, Fe, Co and Ni. *Appl. Surf. Sci.* **2011**, *257*, 2717−2730.
(37) Oku, M.; Tokuda, H.; Hirokawa, K. Final states after Ni2p photoemission in the nickel-oxygen system. *J. Electron Spectrosc. Relat. Phenom.* **1991**, *53*, 201−211.
(38) Azmi, R.; Trouillet, V.; Strafela, M.; Ulrich, S.; Ehrenberg, H.; Bruns, M. Surface Analytical Approaches to Reliably Characterize Lithium Ion Battery Electrodes. *Surf. Interface Anal.* **2018**, *50*, 43−51.
(39) Grosvenor, A. P.; Biesinger, M. C.; Smart, R. St. C.; McIntyre, N. S. New interpretations of XPS spectra of nickel metal and oxides. *Surf. Sci.* **2006**, *600*, 1771−1779.
(40) Kövér, L.; Uda, M.; Cserny, I.; Tóth, J.; Végh, J.; Varga, D.; Ogasawara, K.; Adachi, H. Chemical effects on F KLL Auger spectra in fluorides. *J. Vac. Sci. Technol., A* **2001**, *19*, 1143−1149.
(41) Galakhov, V. R.; Demeter, M.; Bartkowski, S.; Neumann, M.; Ovechkina, N. A.; Kurmaev, E. Z.; Lobachevskaya, N. I.; Mukovskii, Y. M.; Mitchell, J.; Ederer, D. L. Mn 3s Exchange Splitting in Mixed-Valence Manganites. *Phys. Rev. B* **2002**, *65*, No. 113102.
(42) Schulz, N.; Hausbrand, R.; Wittich, C.; Dimesso, L.; Jaegermann, W. XPS-Surface Analysis of SEI Layers on Li-Ion Cathodes: Part II. SEI-Composition and Formation inside Composite Electrodes. *J. Electrochem. Soc.* **2018**, *165*, A833−A846.
(43) Lin, F.; Markus, I. M.; Nordlund, D.; Weng, T.-C.; Asta, M. D.; Xin, H. L.; Doeff, M. M. Surface Reconstruction and Chemical Evolution of Stoichiometric Layered Cathode Materials for Lithium-Ion Batteries. *Nat. Commun.* **2014**, *5*, No. 3529.
(44) Lang, M.; Darma, M. S. D.; Kleiner, K.; Riekehr, L.; Mereacre, L.; Avila, M.; Liebau, V.; Ehrenberg, H. Post Mortem Analysis of Fatigue Mechanisms in $LiNi_{0.8}Cu_{0.15}Al_{0.05}O_2$-$LiNi_{0.5}Co_{0.5}Mn_{0.3}O_2$-$LiMn_2O_4$/Graphite Lithium Ion Batteries. *J. Power Sources* **2016**, *326*, 397−409.
(45) Biesinger, M. C. Advanced Analysis of Copper X-ray Photoelectron Spectra. *Surf. Interface Anal.* **2017**, *49*, 1325−1334.
(46) Le Bail, A.; Duroy, H.; Fourquet, J. L. Ab-initio Structure Determination of $LiSbWO_6$ by X-ray Powder Diffraction. *Mater. Res. Bull.* **1988**, *23*, 447−452.
(47) Schuster, S. F.; Bach, T.; Fleder, E.; Müller, J.; Brand, M.; Sextl, G.; Jossen, A. Nonlinear Aging Characteristics of Lithium-Ion Cells Under Different Operational Conditions. *J. Energy Storage* **2015**, *1*, 44−53.
(48) Stiaszny, B.; Ziegler, J. C.; Krauß, E. E.; Zhang, M.; Schmidt, J. P.; Ivers-Tiffee, E. Electrochemical Characterization and Post-Mortem Analysis of aged $LiMn_2O_4$-NMC/Graphite Lithium Ion Batteries Part II: Calendar Aging. *J. Power Sources* **2014**, *258*, 61−75.

https://dx.doi.org/10.1021/acsomega.0c02174
ACS Omega 2020, 5, 22861−22873